The Astrophysical Journal Letters, 882:L19 (5pp), 2019 September 10 https://doi.org/10.3847/2041-8213/ab3c63

Radio Continuum Emission from Local Analogs of High-z Faint LAEs: Blueberry Galaxies

Biny Sebastian and Omkar Bait
National Centre for Radio Astrophysics, Tata Institute of Fundamental Research, Post Bag 3, Ganeshkhind, Pune 411007, India; biny@ncra.tifr.res.in
Received 2019 May 13; revised 2019 August 15; accepted 2019 August 16; published 2019 September 6

Abstract

We present a radio continuum study of a population of extremely young and starburst galaxies, termed as blueberries at ∼1 GHz using the upgraded Giant Metrewave Radio Telescope. We find that their radio-based star formation rate (SFR) is suppressed by a factor of ∼3.4 compared to the SFR based on optical emission lines. This might be due to (i) the young ages of these galaxies as a result of which a stable equilibrium via feedback from supernovae has not yet been established; (ii) escape of cosmic-ray electrons via diffusion or galactic-scale outflows. The estimated nonthermal fraction in these galaxies has a median value of ∼0.49, which is relatively lower than that in normal star-forming galaxies at such low frequencies. Their inferred equipartition magnetic field has a median value of 27 μG, which is higher than those in more evolved systems like spiral galaxies. Such high magnetic fields suggest that small-scale dynamo rather than large-scale dynamo mechanisms might be playing a major role in amplifying magnetic fields in these galaxies.

Key words: galaxies: dwarf – galaxies: high-redshift – galaxies: ISM – galaxies: magnetic fields – galaxies: starburst – galaxies: star formation

1. Introduction

In the hierarchical galaxy formation model, dwarf galaxies are the first galaxies to have formed stars in the universe. These galaxies are then thought to have undergone various events of mergers and accretion that transformed them into the massive galaxies we observe today. Of these high-redshift galaxy populations, Lyα emitters (LAEs) are of particular interest. Most of the high-z LAEs are star-forming galaxies with low mass, low metallicity, low dust extinction, young stellar population ($\leqslant$100 Myr), and compact sizes (e.g., Gawiser et al. 2007; Malhotra et al. 2012). Studies have also shown that faint dwarf starburst galaxies, a subset of which could be LAEs, can leak a significant amount of Lyman continuum (LyC) photons that could be major contributors for reionization (e.g., Dressler et al. 2015; Drake et al. 2017). Thus, it is important to do a statistical study on the complex processes of star formation (SF), gas accretion, and feedback in these high-z LAEs. But owing to their high redshifts it can be extremely difficult to study them in detail.

Due to these limitations, it is very useful to search for local analogs of high-z LAEs, e.g., the bright green and compact (typically $\leqslant$5 kpc) galaxies termed as "green pea" galaxies (Cardamone et al. 2009) discovered by the volunteers from the Galaxy Zoo project. These galaxies have extremely high star formation rates (SFRs), low stellar masses, low metallicities, and a bright green color due to extremely strong [O III] emission lines. Green-pea galaxies are also known to leak a significant amount of LyC photons that can ionize the surrounding intergalactic medium (e.g., Izotov et al. 2016). Yang et al. (2017) have searched for low-redshift counterparts of the green-pea galaxies in the Sloan Digital Sky Survey (SDSS) *ugriz* broadband images. They have found a sample of 40, spectroscopically confirmed, starburst dwarf galaxies with even smaller sizes ($\leqslant$1 kpc), lower stellar masses, and low metallicities, termed "blueberry" galaxies. They are supposed to be the local analogs of high-z faint LAEs (Yang et al. 2017).

A complementary study of this peculiar population of galaxies at radio frequencies can provide an independent estimate of their total (dust-obscured and unobscured) SFRs (e.g., Condon 1992; Magnelli et al. 2015; Pannella et al. 2015; Bera et al. 2018). Radio emission from high-redshift ($z \sim 3-4$) Lyman-break galaxies (LBGs) has been reported only by stacking analysis, (e.g., Carilli et al. 2008; Ho et al. 2010; To et al. 2014). This stacked radio luminosity was also found to be systematically lower than those expected from the ultraviolet (UV) luminosity (Carilli et al. 2008). However, for such galaxies, it is hard to separate the effect of an increased inverse Compton (IC) cooling of the relativistic electrons due to scattering from cosmic microwave background (CMB) photons versus an intrinsic deficit. The local analogs of LBGs and LAEs will have a negligible amount of IC-CMB losses and are also easier to detect. However, in a previous study on green peas, a direct detection in radio was found only for two of them using the Giant Metrewave Radio Telescope (GMRT; Chakraborti et al. 2012).

In this Letter, we push these radio studies to the even younger and lower-mass population of blueberry galaxies. We report their first-ever radio detections, which has been possible due to the wideband backend of the upgraded GMRT (uGMRT; Gupta et al. 2017) allowing us to reach an rms of ∼15 μJy beam^{-1} with reasonable integration time at 1.25 GHz (Section 2). Here we compare their radio-based SFRs with the optical SFR and estimate their nonthermal fraction and equipartition magnetic field strengths.

Throughout this Letter, we use the standard concordance cosmology from WMAP9 (Hinshaw et al. 2013) with $\Omega_M = 0.286$, $\Omega_\Lambda = 0.714$, and $h_{100} = 0.69$.

2. GMRT Observations

2.1. Sample

In this pilot study, we selected a subset of the 40 confirmed blueberry galaxies from Yang et al. (2017) as follows. The

Table 1
Sample and Observation Details

ObjID[a]	R.A. (deg)	Decl. (deg)	Redshift[b] z	Time on Source (hours)	Flux Density (μJy)	Beam Size ($'' \times ''$)	Beam P.A. (°)
27	$01^h46^m53\overset{s}{.}307$	$+03^d19^m22\overset{s}{.}360$	0.047	1.97	105 ± 15	$6\overset{''}{.}87 \times 3\overset{''}{.}24$	$71\overset{\circ}{.}96$
34	$03^h57^m13\overset{s}{.}516$	$+18^d08^m45\overset{s}{.}582$	0.037	1.97	70 ± 14	$3\overset{''}{.}04 \times 2\overset{''}{.}48$	$88\overset{\circ}{.}50$
3	$08^h25^m40\overset{s}{.}449$	$+18^d46^m17\overset{s}{.}209$	0.038	1.75	72 ± 11	$3\overset{''}{.}30 \times 2\overset{''}{.}51$	$77\overset{\circ}{.}96$
5	$10^h32^m56\overset{s}{.}727$	$+49^d19^m47\overset{s}{.}226$	0.044	1.51	<39[c]	$4\overset{''}{.}23 \times 2\overset{''}{.}40$	$75\overset{\circ}{.}81$
66	$11^h13^m12\overset{s}{.}241$	$+03^d01^m12\overset{s}{.}831$	0.023	1.64	56 ± 15	$3\overset{''}{.}39 \times 2\overset{''}{.}42$	$-10\overset{\circ}{.}31$
67	$11^h23^m48\overset{s}{.}949$	$+20^d50^m31\overset{s}{.}297$	0.033	1.86	373 ± 17	$3\overset{''}{.}88 \times 2\overset{''}{.}31$	$87\overset{\circ}{.}74$
6	$13^h23^m47\overset{s}{.}462$	$-01^d32^m52\overset{s}{.}008$	0.023	1.74	91 ± 18	$2\overset{''}{.}59 \times 2\overset{''}{.}43$	$49\overset{\circ}{.}60$
10	$15^h09^m34\overset{s}{.}173$	$+37^d31^m46\overset{s}{.}117$	0.033	1.81	345 ± 16	$3\overset{''}{.}14 \times 2\overset{''}{.}55$	$-69\overset{\circ}{.}71$
12	$15^h56^m24\overset{s}{.}474$	$+48^d06^m45\overset{s}{.}792$	0.050	1.99	107 ± 12	$3\overset{''}{.}20 \times 2\overset{''}{.}36$	$-41\overset{\circ}{.}99$
13	$16^h08^m10\overset{s}{.}363$	$+35^d28^m09\overset{s}{.}346$	0.033	2.16	58 ± 17	$7\overset{''}{.}32 \times 3\overset{''}{.}31$	$55\overset{\circ}{.}38$

Notes.
[a] The ObjIDs correspond to those from Yang et al. (2017).
[b] The redshifts are taken from Yang et al. (2017).
[c] 3σ upper limit on the flux density.

SFRs from Yang et al. (2017) were used to calculate the expected nonthermal flux density at 1.4 GHz for a normal star-forming galaxy following Yun & Carilli (2002). Since this calibration can vary for our population of young starburst galaxies, we selected 10 of the brightest sources to ensure direct detections.

These galaxies were observed using uGMRT (project ID: 34_123) at Band 5 (1000–1450 MHz). The details of the observations are listed in Table 1.

2.2. Data Analysis

Basic editing and calibration of the data were carried out using standard procedures in AIPS. Data corrupted by RFI were identified and removed using automatic flagging algorithms in AIPS. We carried out flux, phase, and bandpass calibration using standard calibrators. The flux calibrators used were 3C 147, 3C 286, and 3C 48. The time resolution used for this observation was 10.1 s and no further time averaging was carried out. Few channels were then averaged using task "SPLAT" in AIPS, which resulted in a final channel width of ~3.5 MHz. This channel width would lead to a 3% reduction in the flux 5′ away from the center of the field due to bandwidth smearing, whereas at the location of our target, there will only be negligible errors. The calibrated target source was then extracted out of the main data set. Initial rounds of imaging and self-calibration were carried out in AIPS using only a central bandwidth of 100 MHz to make sure bandwidth effects do not adversely affect the image quality. Four rounds of the phase-only self-calibration were carried out in AIPS to remove antenna based ionospheric errors. The target source was then exported to CASA and imaged using the MS-MFS algorithm (Rau & Cornwell 2011). The flux densities of the target sources were then estimated using the "JMFIT" task in AIPS. The flux density values of all the sources in our sample are summarized in Table 1. The errors on flux density quoted in Table 1 represent the rms from the images. However, for all the rest of the calculations we add a 10% calibration error on the flux density in quadrature. We found detections for 9 of the 10 sources in our sample. Figure 1 shows the contours of radio images of these nine sources overlaid on the *grz*-band color composite image from the Dark Energy Camera Legacy Survey (DECaLS) or the Mayall *z*-band Legacy Survey (MzLS; Dey et al. 2019). We used the *gri* bands from SDSS (Abazajian et al. 2009) in the case of the source, ObjID-34 due to the unavailability of DECaLS or MzLS images.

3. Results

Normal star-forming galaxies show a tight correlation between the SFR and nonthermal radio emission and typically have a negligible amount of thermal emission at frequencies of ~1 GHz and below (~10% ± 9%; e.g., Tabatabaei et al. 2017). Here we investigate the SFR derived from the radio continuum emission for our sample of the blueberry galaxies and compare it with the SFR derived using optical emission lines.

The radio-based SFRs for our sample are derived using the 1.4 GHz luminosity calibration from Murphy et al. (2011, Equation (17)). For our sample of blueberries, the median value of the SFR from this calibrator is 0.15 $M_\odot$ yr^{-1}. In Figure 2 we plot the radio SFR against the SFR derived using the Hα line from Yang et al. (2017). Although there is a correlation between the two SFRs, the SFRs estimated from the radio emission are significantly lower than the ones deduced from Hα. Both the SFR calibrators use Kroupa initial mass function (IMF) with the same stellar mass limits (0.1 $M_\odot$–100 $M_\odot$). Hence, we do not expect any difference in the two SFRs due to a difference in the IMF and/or it is adopted stellar mass range. Note that here and in all other further analysis we do not use ObjID 5 (red star) since it was not detected in our observation and hence does not have a reliable flux measurement. We do a least-squares fit between the $\mathrm{SFR}_{1.4\ \mathrm{GHz}}$ and $\mathrm{SFR}_{\mathrm{H}\alpha}$, which has a slope of 0.297 ± 0.028. This factor can be used to correct the radio-based SFRs of blueberries. The scatter in the residual after removing the best-fit line is 0.065. Note that the 3σ upper limit of the undetected source, ObjID 5, also lies within the 2σ scatter of this relation. Blueberries can be dust obscured (Rong et al. 2018), which could mean that the $\mathrm{SFR}_{\mathrm{H}\alpha}$ needs some dust correction. However, it will only further enhance the radio suppression observed here.

The stacking detection of green-pea galaxies with the VLA FIRST data showed suppression of radio continuum emission by a factor of ~0.53 (Chakraborti et al. 2012); however, the individual detections were closer to the expected values. Carilli et al. (2008) also find a depression in the stacked radio continuum emission for a sample of high-*z* LBGs. They proposed that such a reduction can be a result of increased IC-

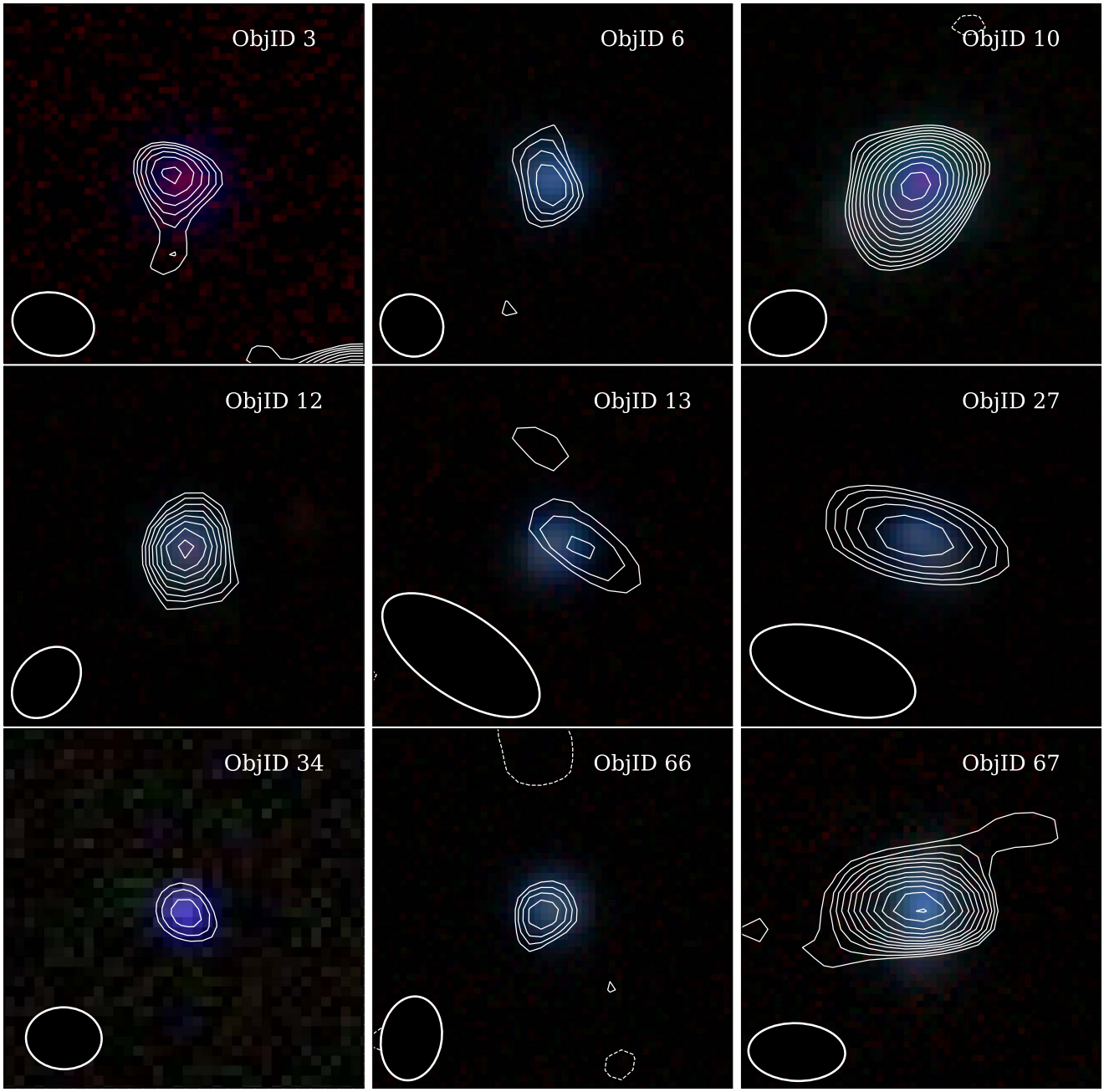

Figure 1. Contours of the 1.25 GHz continuum image overlaid on the optical *grz*-band color composite image ($14\farcs4 \times 14\farcs4$ in size) from DECaLS or MzLS (for sources without DECaLS data) or SDSS (for sources without DECaLS or MzLS data). The contour levels represent $3\sigma \times (-1.0, 1.0, 1.19, 1.41, 1.68, 2.0, 2.38, 2.83, 3.36, 4.0, 4.76, 5.66, 6.73, 8.0, 9.51, 11.31)$ μ Jy beam^{-1} where $\sigma = 11.0, 13.0, 18.0, 16.0, 12.0, 14.3, 15.0, 14.0, 10.0, 20.0$ for each of the sources sorted in the ascending order of their ObjIDs. The clean beam is shown in the bottom left corner of each cutout.

CMB losses at high-z or a combination of IC-CMB losses and intrinsic reduction in radio continuum. Our sample of blueberry galaxies are at very low redshifts and the effects of IC-CMB are negligible, which implies that the suppression is intrinsic. And it is possible that even the high-z LBGs show an intrinsic suppression of radio continuum. One reason for the diminished radio emission might be the young age itself. Greis et al. (2017) point out that the standard SFR calibrators depend upon the stellar population age and SF history. Hα emission traces the recent SF ($\sim$10 Myr), whereas the synchrotron or nonthermal radio emission traces SF that has been continuing for about 100 Myr. Another reason for the diminished radio emission could be that the relativistic electrons produced in the galaxy escape from these galaxies easily compared to other massive systems due to their shallow gravitational potential (Greis et al. 2017).

In both the above cases, only the nonthermal radio emission will show a decrement in the flux densities. Hence, the thermal radio emission should be consistent with that deduced using emission lines. Tabatabaei et al. (2017) provide a calibration for converting the thermal radio emission to SFR using the KINGFISH galaxy sample (Kennicutt et al. 2011). Under this assumption, we can estimate the nonthermal fraction as follows. Let δ be the thermal fraction such that the thermal luminosity at the L band ($L_{\rm th}$) is δ times the total observed radio luminosity at the L band ($L_{\rm tot}$). And let β be the thermal radio

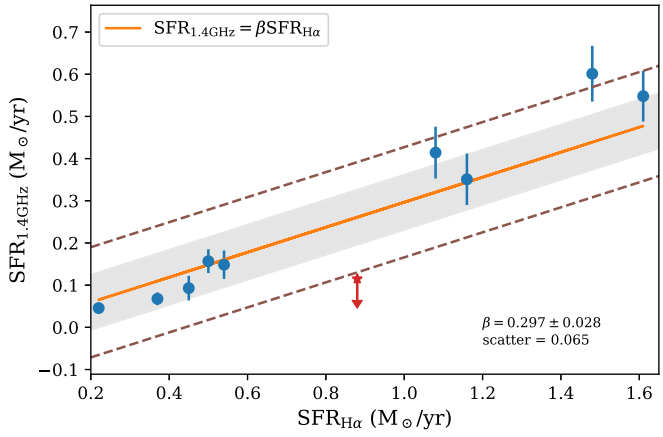

Figure 2. Comparison of SFRs from Hα and 1.4 GHz radio luminosity shown as blue points. The red star corresponds to the 3σ upper limit on the SFR for one of the nondetection in our sample. The least-squares fit between the two SFRs (yellow solid line) has a slope of 0.297 ± 0.028. The scatter in the residual, obtained after subtracting the best-fit line, is 0.065 (gray shaded region). The dashed line shows the 2σ scatter of the residual.

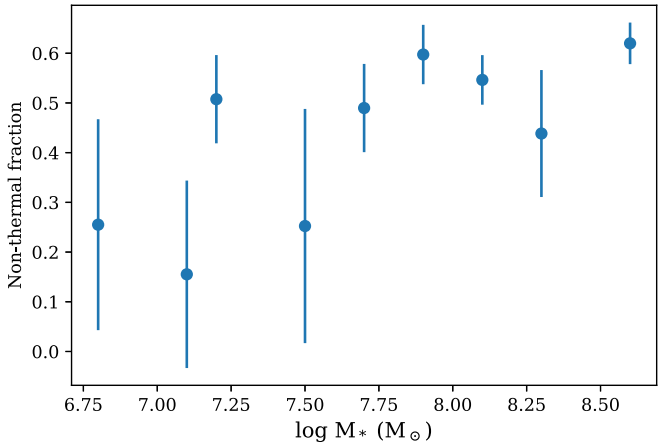

Figure 3. Estimated nonthermal fraction as a function of stellar mass for our sample of blueberry galaxies.

calibration factor used to estimate the SFR from Tabatabaei et al. (2017). We can then relate the SFR from Hα emission and δ as $\mathrm{SFR_{H\alpha}} = \mathrm{SFR_{th}} = \beta \times (L_{\mathrm{th}}) = \beta \times (\delta L_{\mathrm{tot}})$. The nonthermal fraction, which is nothing but (1-δ), can the be estimated using this above relation.

The median value of the nonthermal fraction for our sample of blueberry galaxies is ∼0.49. Such a low nonthermal fraction was also previously observed in other types of dwarf galaxies, e.g., in blue compact dwarfs (Thuan et al. 2004; Ramya et al. 2011), in IC 10, a poststarbust dwarf irregular galaxy (Heesen et al. 2011) and sample of faint star-forming dwarf galaxies (Roychowdhury & Chengalur 2012). Greis et al. (2017) showed that the fraction of thermal radio emission can be as high as ∼100% for a sample of local Lyman-break analogs (LBAs).

The difference in the nonthermal fraction in a sample of dwarf galaxies with that of normal galaxies suggests that there might be an evolution of the nonthermal fraction with the growth of galaxies, particularly in their stellar mass. We explore this in our sample by plotting the nonthermal fraction against the galaxy stellar mass in Figure 3. We see some correlation between the nonthermal fraction and stellar mass. The Spearman's rank correlation coefficient between the two variables is 0.68 (with a p value of 0.04). However, given that the uncertainties in this fraction are large and our sample is small, we only claim a tentative correlation.

The origin of the nonthermal radio emission is attributed to the supernovae (SNe) shocks where the cosmic-ray electrons (CREs) are generated and the magnetic fields amplified. We estimate the magnetic fields from the nonthermal flux density values in these galaxies. We make use of the revised formula given by Beck & Krause (2005) for calculating the equipartition magnetic fields. We assume the ratio of the relativistic proton number density to that of the electrons to be equal to 100 and a spectral index value of −0.7. We assume a path length of 0.3 kpc following Chakraborti et al. (2012). The median equipartition magnetic field for our sample is estimated to be ∼27 μG.

4. Discussion

To identify the reason for the deficit and the evolution in the radio nonthermal emission we compare the characteristic timescales of various processes (age of the recent starburst, buildup of SN rate, and CRE escape via diffusion or outflows).

4.1. Young Ages

Assuming that most of the stellar mass was built up in the starburst phase, we can use the current SFR to put an upper limit on the time elapsed since the onset of this burst. We find that this timescale ranges from 30 to 370 Myr with a median value of 70 Myr for our sample of galaxies. Greis et al. (2017) show using a stellar population synthesis for a system that forms stars at a rate of $1\,M_{\odot}\ \mathrm{yr}^{-1}$ that the SFR traced by Hα and [O II] becomes significant just after the SF commences, whereas the synchrotron emission takes about 10 Myr to become significant and matches with the optical-based SFRs only after 100 Myr after the onset of SF. Thermal emission, on the other hand, traces the SFR on timescales similar to Hα and [O II].

Even the evolution of the nonthermal fraction (see Figure 3) can be easily explained if the decrement is due to young age. The bolometric nonthermal emission, L^{NT}, from a galaxy can be roughly calculated as $L^{\mathrm{NT}} = \nu_{\mathrm{CCSNe}} \times E_{\mathrm{el}}$ (Bressan et al. 2002), where ν_{CCSN} is the rate of the occurrence of CCSNe and E_{el} is the power emitted by an electron via synchrotron losses times the lifetime of the electron. There is an overall dependence of the nonthermal emission on the magnetic field since E_{el} also depends on the magnetic field. Greis et al. (2017) consider only the evolution in the rate of CCSNe, which stabilizes after about 10 Myr but the magnetic field could be evolving for a longer timescale. Schleicher et al. (2010) suggest that saturation of magnetic fields amplified via a small-scale dynamo (SSD; which could be the preferred model for blueberries) happens only after ∼100 Myr. Hence, the magnetic fields in our sample of blueberry galaxies might still be in the evolutionary phase, as a result of which the nonthermal fraction shows an evolution.

Thus, in blueberry galaxies, which form one of the youngest classes of star-forming galaxies (with median ages ⩽70 Myr), it is plausible that the SF has not been sustained long enough for synchrotron emission to become dominant.

4.2. CRE Escape via Diffusion/Outflows

The deficit in the nonthermal radio emission can also be explained by the escape of CREs via diffusion and/or winds/outflows. This happens only if their timescales are lower than

the synchrotron-loss timescales (Carilli et al. 2008). Diffusion timescale (t_D) can be estimated as $t_D = \frac{R^2}{D}$, where D, the diffusion coefficient, is equal to $\frac{l_0 c}{3}$ and R is the size of the galaxy. The typical values of the mean free path $l_0 = 0.3$ kpc (see Chakraborti et al. 2012 and Calvez et al. 2010 for details). For an upper limit of 1 kpc on the size we put an upper limit of 0.033 Myr on t_D. We estimate the synchrotron-loss timescales using the relation $\tau_{\rm syn} = 33.4 B_{10}^{-\frac{3}{2}} \nu_1^{-\frac{1}{2}}$ Myr (Pérez-Torres & Alberdi 2007), where B_{10} is the magnetic field value in units of 10 μG, and ν_1 is the critical frequency in GHz. For a critical frequency value of 1.25 GHz, the synchrotron-loss timescales turn out to be ~6.7 Myr. Since $t_D \ll \tau_{\rm syn}$, CRE diffusion might be playing a major role in the suppression of radio continuum emission in these galaxies.

Another possibility is the escape of CREs due to winds or outflows. Galactic superwinds were shown to be present in all the galaxies which had global SFR densities (SFRDs) greater than 0.1 $M_\odot$ yr^{-1} kpc^{-2} (Heckman 2002). Assuming an upper limit of 1 kpc for the size of these blueberry galaxies, the SFRDs of all the galaxies are higher than 0.1 $M_\odot$ yr^{-1} kpc^{-2}. The typical wind terminal velocities attained in starbursting galaxies hosting superwind are in the range, 2000–3000 km s^{-1} (Heckman et al. 1990). Assuming a wind velocity of 2000 km s^{-1}, and a galaxy size of 1 kpc, we obtain escape timescales of 0.5 Myr, which are also lower than the synchrotron-loss timescales. Such an outflow would only be a natural consequence of the massive SF that is happening in these young massive galaxies.

In our study, we are not able to distinguish between the different scenarios that lead to the decrement in the radio continuum emission.

4.3. Amplification of Magnetic Fields

The magnetic fields for our galaxies are much higher than those seen in more evolved systems like normal spiral galaxies (e.g., about 9 ± 2 μG; Niklas 1995).

The magnetic field amplification is explained widely using the dynamo mechanism. The large-scale dynamo models can effectively convert the kinetic energy to magnetic energy in spiral galaxies where differential rotation of conducting fluid is present. However, blueberry galaxies are much younger and do not yet possess the kind of large-scale differential rotation seen in spirals. SSD models, on the other hand, amplify the magnetic field by converting turbulent energy due to supernova shocks (Ferrière & Blanc 1996) to the magnetic energy at much smaller scales. Moreover, the growth rates predicted by SSD models are larger compared to the large-scale dynamo models (Brandenburg & Subramanian 2005). Hence, the SSD mechanism is often invoked to explain the μG level magnetic fields observed in young galaxies (Kulsrud et al. 1997; Rieder & Teyssier 2015). Our study also favors SSD mechanism for the amplification of magnetic fields compared to the large-scale dynamo models. A study of the evolution of magnetic fields with the stellar mass in such systems can provide useful insights into the underlying mechanisms that amplify the magnetic fields.

In the future, we aim to do detailed radio spectral modeling (Klein et al. 2018) to make accurate estimates of the thermal/nonthermal fraction and as a result, the magnetic field. In the case where CREs escape the galaxy and causes the decrement in the radio emission, it would show a break in the radio synchrotron spectrum (Lisenfeld et al. 2004; Klein et al. 2018). We would also increase the sample size to include both the lower-mass and higher-mass galaxies (green-pea galaxies) to study the evolution of the nonthermal properties in these systems. We also aim to do a detailed comparison of SFRs from different indicators (e.g., UV+IR, Hα, radio flux density, and multiwavelength spectral energy distribution fitting).

We thank the anonymous referee for insightful comments that helped in improving the article significantly. We also thank S. Kurapati, A. Bera, and S. Manna for several of their suggestions and comments. We thank the staff of the GMRT who have made these observations possible. The GMRT is run by the National Center for Radio Astrophysics of the Tata Institute of Fundamental Research.

ORCID iDs

Biny Sebastian https://orcid.org/0000-0001-8428-6525
Omkar Bait https://orcid.org/0000-0003-2722-8841

References

Abazajian, K. N., Adelman-McCarthy, J. K., Agüeros, M. A., et al. 2009, ApJS, 182, 543
Beck, R., & Krause, M. 2005, AN, 326, 414
Bera, A., Kanekar, N., Weiner, B. J., Sethi, S., & Dwarakanath, K. S. 2018, ApJ, 865, 39
Brandenburg, A., & Subramanian, K. 2005, PhR, 417, 1
Bressan, A., Silva, L., & Granato, G. L. 2002, A&A, 392, 377
Calvez, A., Kusenko, A., & Nagataki, S. 2010, PhRvL, 105, 091101
Cardamone, C., Schawinski, K., Sarzi, M., et al. 2009, MNRAS, 399, 1191
Carilli, C. L., Lee, N., Capak, P., et al. 2008, ApJ, 689, 883
Chakraborti, S., Yadav, N., Cardamone, C., & Ray, A. 2012, ApJL, 746, L6
Condon, J. J. 1992, ARA&A, 30, 575
Dey, A., Schlegel, D. J., Lang, D., et al. 2019, AJ, 157, 168
Drake, A. B., Garel, T., Wisotzki, L., et al. 2017, A&A, 608, A6
Dressler, A., Henry, A., Martin, C. L., et al. 2015, ApJ, 806, 19
Ferrière, K. M., & Blanc, M. 1996, JGR, 101, 19871
Gawiser, E., Francke, H., Lai, K., et al. 2007, ApJ, 671, 278
Greis, S. M. L., Stanway, E. R., Levan, A. J., Davies, L. J. M., & Eldridge, J. J. 2017, MNRAS, 470, 489
Gupta, Y., Ajithkumar, B., Kale, H., et al. 2017, CSci, 113, 707
Heckman, T. M. 2002, in ASP Conf. Ser. 254, Extragalactic Gas at Low Redshift, ed. J. S. Mulchaey & J. T. Stocke (San Francisco, CA: ASP), 292
Heckman, T. M., Armus, L., & Miley, G. K. 1990, ApJS, 74, 833
Heesen, V., Rau, U., Rupen, M. P., Brinks, E., & Hunter, D. A. 2011, ApJL, 739, L23
Hinshaw, G., Larson, D., Komatsu, E., et al. 2013, ApJS, 208, 19
Ho, I.-T., Wang, W.-H., Morrison, G. E., & Miller, N. A. 2010, ApJ, 722, 1051
Izotov, Y. I., Orlitová, I., Schaerer, D., et al. 2016, Natur, 529, 178
Kennicutt, R. C., Calzetti, D., Aniano, G., et al. 2011, PASP, 123, 1347
Klein, U., Lisenfeld, U., & Verley, S. 2018, A&A, 611, A55
Kulsrud, R. M., Cen, R., Ostriker, J. P., & Ryu, D. 1997, ApJ, 480, 481
Lisenfeld, U., Wilding, T. W., Pooley, G. G., & Alexander, P. 2004, MNRAS, 349, 1335
Magnelli, B., Ivison, R. J., Lutz, D., et al. 2015, A&A, 573, A45
Malhotra, S., Rhoads, J. E., Finkelstein, S. L., et al. 2012, ApJL, 750, L36
Murphy, E. J., Condon, J. J., Schinnerer, E., et al. 2011, ApJ, 737, 67
Niklas, S. 1995, PhD thesis, Univ. Bonn
Pannella, M., Elbaz, D., Daddi, E., et al. 2015, ApJ, 807, 141
Pérez-Torres, M. A., & Alberdi, A. 2007, MNRAS, 379, 275
Ramya, S., Kantharia, N. G., & Prabhu, T. P. 2011, ApJ, 728, 124
Rau, U., & Cornwell, T. J. 2011, A&A, 532, A71
Rieder, M., & Teyssier, R. 2015, IAUGA, 22, 2243950
Rong, Y., Yang, H., Zhang, H.-x., et al. 2018, arXiv:1806.10149
Roychowdhury, S., & Chengalur, J. N. 2012, MNRAS, 423, L127
Schleicher, D. R. G., Banerjee, R., Sur, S., et al. 2010, A&A, 522, A115
Tabatabaei, F. S., Schinnerer, E., Krause, M., et al. 2017, ApJ, 836, 185
Thuan, T. X., Hibbard, J. E., & Lévrier, F. 2004, AJ, 128, 617
To, C.-H., Wang, W.-H., & Owen, F. N. 2014, ApJ, 792, 139
Yang, H., Malhotra, S., Rhoads, J. E., & Wang, J. 2017, ApJ, 847, 38
Yun, M. S., & Carilli, C. L. 2002, ApJ, 568, 88